A Mathematical Framework for Indeterminacy in Parabolic PDEs: The Neutrosophic Heat Equation

Ghassan AL-Thabhawee[1], Hussein Alkattan[2,3], El-Sayed M. El-kenawy[4,5,*], Marwa M. Eid[6,7]

[1]Sciences of Mathematics, Computer Sciences, College of Health and Medical Techniques-Kufa Al-Furat Al-Awsat Technical University, Kufa, Iraq

[2]Department of System Programming, South Ural State University, Chelyabinsk, Russia

[3]Directorate of Environment in Najaf, Ministry of Environment, Najaf, Iraq

[4]Delta Higher Institute of Engineering and Technology Department for Communications and Electronics Mansoura 35511, Egypt

[5]Applied Science Research Center. Applied Science Private University, Amman, Jordan

[6] Faculty of Artificial Intelligence, Delta University for Science and Technology, Mansoura, Egypt

[7]Jadara Research Center, Jadara University, Irbid 21110, Jordan

Emails: gmohammed@atu.edu.iq; alkattan.hussein92@gmail.com; skenawy@ieee.org; mmm@ieee.org

Abstract

We develop a neutrosophic framework for the 1-D transient heat equation that treats key thermal parameters as indeterminate rather than fixed or strictly probabilistic. Thermal diffusivity and source strength are represented by neutrosophic intervals; two extreme forward solves yield guaranteed envelopes u_{min} and u_{max}, from which we compute a core field $u_{mean} = \frac{1}{2}(u_{min} + u_{max})$, an absolute width $W = u_{max} - u_{min}$, and a relative indeterminacy index $I = W/(|u_{mean}| + \varepsilon)$. Using an explicit FTCS discretization with stability enforced by α_{max}, we report decision-oriented diagnostics: spatio-temporal maps of u_{mean}, W, and I; band plots along space/time sections; percentile trajectories of I over time; coverage curves quantifying the fraction of space-time with $I \leq \tau$; and response surfaces showing sensitivity of $u(x^*, T)$ to (α, S). Results demonstrate that, even when absolute spreads remain small, localized reliability losses can occur where u_{mean} crosses zero, a regime routinely obscured by point-estimate modelling. The framework is transparent (envelopes + core), computationally light (two extreme runs), and compatible with neutrosophic statistics for data-driven interval setting. Beyond thermal diffusion, the method provides a conservative, explainable backbone for transport-driven decisions in materials, interfaces, and infrastructure subject to incomplete or evolving information.

Keywords: Neutrosophic modeling; Heat equation; Transient heat conduction; Interval uncertainty; Envelope propagation; Relative indeterminacy index (RII); Thermal diffusivity; Source amplitude; Uncertainty quantification

1. Introduction

Accurate predictions of heat transfer are key to materials and devices under extreme or rapidly changing conditions ceramic thermal-barrier components, high-heat-flux synchrotron beamline optics, metal ceramic interfaces, conductive composites, and even pavement systems exposed to thermal cycling. Yet in all of these contexts, the inputs to the heat equation thermal diffusivity, heat capacity, contact resistance, and distributed sources are typically partially unknown, temperature-dependent, or batch-to-batch and time-varying. Examples are typical thermal-shock tests of advanced ceramics, where material curves are highly sensitive to temperature and microstructure [2]; high-temperature electromagnetic/thermal composites such as SiBCN-ceramic-shielded

DOI: https://doi.org/10.54216/IJNS.270127

graphene and MXene conductors, where effective conductivity over operating regimes is affected by oxidation resistance and percolation [3], [7]; porous insulators whose conductivity is a function of clay fraction and sintering temperature [4]; and C/C-Inconel contacts, for which the thermal contact resistance at high temperature is both the deciding and notoriously erratic parameter [6]. On the systems side, high-heat-flux beamlines must have conservative thermal envelopes in order to be survivable in the presence of uncertain loads and contact conditions [5]. In short, indeterminacy imprecision, partial truth, and changing conditions is the rule, not the exception.

Traditional cures are inadequate. Point-estimate models mask uncertainty and can make brittle recommendations if the "nominal" parameter set is slightly in error. Fully probabilistic solutions can be strong, but they need distributional assumptions and richness in data that most labs or field deployments do not possess. A practical alternative is to model what is called admissible sets intervals that enclose reasonable parameter values and propagate these sets through the governing physics to acquire conservative state envelopes, along with a central tendency and reliability diagnostics. This is precisely the organizing idea in neutrosophic logic and statistics, which formalize reasoning under indeterminacy and established merit in fields where data are incomplete, imprecise, or heterogeneous [10]-[15], [16]-[23], [24]-[27]. Neutrosophic ideas have enabled hypothesis testing with fuzzy data [10], measure/probability theory bases [11], research approach [15], and applied analytics from medical decision-making support [13] to document abstraction [19], pandemic data analysis [18], and geophysical clustering [16]. In metrology-type setups, neutrosophic sampling schemes, variance-homogeneity tests, and outlier identification provide decision-making procedures that avoid spurious certainty yet remain functional [22], [26], [27].

This article positions the heat equation as an open, physics-informed laboratory for neutrosophic modelling. We take the most significant parameters thermal diffusivity and source-strength coefficient to be neutrosophic intervals and compute: (i) a lower/upper envelope pair from solving the forward problem at corners of the interval, (ii) a core (midpoint) field, and (iii) diagnostics quantifying absolute spread and a relative indeterminacy index (spread normalized by the core magnitude). These outputs are visualized as spatio-temporal heatmaps, time/space "bands," percentile trajectories, coverage curves (fraction of space–time with indeterminacy below some threshold), and basic parameter-response surfaces that convey sensitivity. The process is made accessible to engineers and reviewers: it shows where and when uncertainty matters, and to what extent, before any downstream design, control, or certification decision is made.

The motivation spans materials and sizes. In ceramic thermal shock engineering, elastic property uncertainty and transport that is temperature-dependent has immediate consequence for calculated damage thresholds and safety margins [2]. For MXene and SiBCN-ceramic protected graphene conductors alike, the same element may transition from one regime (from oxidizing to protected, from ordered to defect-rich networks) to another, effectively modifying coupled heat-source conductivity and effective conductivity in ways best described by admissible bounds, not by exact distributions [3], [7]. Porous diatomite-insulator property spreads are regulated by clay content and sintering schedules; extending these spreads to a diffusion model anchors the "best-case" and "worst-case" thermal response [4]. Interface-limited composites (e.g., C/C-Inconel) flourish or die by thermal contact resistance, whose response at high temperatures is a function of surface preparation, pressure, oxidation, and cycling history [6]; envelope propagation restores conservative temperature ranges without the need to know one TCR curve. Even in non-military publications, cold temperature cracking in fiber-reinforced asphalt is caused by interrelating rheology and exposure histories that differ site to site; core-and-spread thermal field reporting helps to correlate climatic risk with pavement performance [8].

Indeterminacy is not only parametric but also scale-dependent and context-dependent. Experiments with metallic nanowires illustrate the validity of the Bloch Grüneisen law for certain regimes of diameter with geometry-dependent scattering, provoking physical models that accommodate more than one admissible parameterization with temperature and size [28]. Microbiological viability on copper surfaces is dependent on gene-mediated resistance pathways that potentially adapt with environmental exposure, effectively changing boundary conditions with time [29]. Neutrosophic statistics wholeheartedly accept such realities: hypothesis tests and estimators are designed to hold under partial truth and vagueness in measurement [10], [22], [26], [27]. The same ethos of confidence without overconfidence is what we apply to the heat equation.

Our contributions are threefold. First, we rigorously formalize a neutrosophic PDE propagation recipe for parabolic problems that is easy to employ on top of standard finite-difference solvers: run the endpoints, compute the midpoint, and return spread and relative indeterminacy. The recipe is bolstered by monotonicity properties of the explicit heat operator and is compatible with temperature-dependent coefficients. Second, we build an illustrative results package that conveys to review and design: core field and indeterminacy maps; bands along slices; temporal percentiles (median, 90th, 99th) indicating how reliability varies; coverage curves which summarise rich spatio-temporal behaviour into one interpretable quantity; and response surfaces over parameter rectangles. Third, we connect this PDE-level transparency to the neutrosophic analytics toolbox sampling plans, variance tests, outliers, similarity metrics, and interval statistics so that lab and design teams can implement a single workflow from raw uncertain data to conservative, interpretable thermal predictions [12]-[14], [18], [19], [22], [24]-[27].

DOI: https://doi.org/10.54216/IJNS.270127

In practice, getting intervals is simple. Handbooks and "crash course" books provide nominal ranges and caution (e.g., rule-of-thumb electronics/thermal properties) accessible to seed acceptable sets where full characterization is not feasible [1]. Exiguitaency literature dispersed in property–temperature curves of a given material system can be condensed into lower and upper envelopes, each bound by separate regimes (oxidation on/off) [2], [3], [7]. Interface attributes like TCR can be bounded on the basis of surface condition and pressure levels from experimental data [6]. Where there are more data available, neutrosophic statistics give interval estimates from measurement directly, including scale effects and anisotropy as for rock-joint roughness studies [24], [25]. In each case, our propagation maps take intervals in as input and deliver envelopes as output with virtually zero modeling overhead.

neutrosophic modelling is an additive, not a replacement, uncertainty methodology. Probabilistic sensitivity and Bayesian calibration are worthwhile when data and assumptions warrant them; robust optimization is appealing for design under worst-case guarantees. Our own argument is narrower and pragmatic: optimize or certify once having observed the physics under genuine bounds. For thermal transport in ceramics, composites, porous structures, interfaces, and roads, the neutrosophic heat-equation model offers a conservative, understandable basis that can be audited and refined as new data become available [2]-[8], [28], [29], [30]. That transparency what the model knows, what it doesn't, and how that indeterminacy spreads throughout space and time is required for reliable engineering decision.

2. Problem Statement

Many thermal systems are governed by the 1-D transient heat equation on a bounded rod $x \in [0,1]$ over a finite horizon $t \in [0,T]$:

$$\frac{\partial u}{\partial t}(x,t) = \alpha \frac{\partial^2 u}{\partial x^2}(x,t) + Sq(x,t), (x,t) \in (0,1) \times (0,T] \quad (1)$$

with temperature $u(x,t)$, thermal diffusivity $\alpha > 0$, and a source amplitude S multiplying a known spatiotemporal pattern $q(x,t)$. The initial and boundary data are

$$u(x,0) = u_0(x), u(0,t) = g_L(t), u(1,t) = g_R(t), t \in [0,T] \quad (2)$$

In many realistic scenarios-new materials, partially calibrated sensors, or transient heating-key parameters are not precisely known. Rather than collapsing this ignorance to point estimates or purely probabilistic models, we adopt a neutrosophic representation of indeterminacy: the admissible values of α and S are encoded as intervals capturing truth-indeterminacy-falsity in an operational way.

$$\alpha \in [\alpha_{min}, \alpha_{max}], S \in [S_{min}, S_{max}] \quad (3)$$

where $[\alpha_{min}, \alpha_{max}]$ and $[S_{min}, S_{max}]$ summarize all credible values given the available evidence. The core problem is to propagate the neutrosophic indeterminacy in (α, S) through the heat dynamics (1)-(2), and to report outputs that are decision-useful-i.e., fields that reflect central behavior, guaranteed bounds, and a local measure of reliability-without imposing unjustified probabilistic structure.

Let $u(x,t;\alpha,S)$ denote the unique classical solution of (1)-(2) for fixed (α,S). Define the extreme (envelope) solutions by evaluating the model at the comers of (3):

$$u_{min}(x,t) := u(x,t;\alpha_{min},S_{min}), u_{max}(x,t) := u(x,t;\alpha_{max},S_{max}) \quad (4)$$

(Under the monotonicity of the parabolic operator with respect to α and the linearity in S for nonnegative q. these extremes provide order-consistent bounds; if q changes sign, the same construction remains conservative for the set of admissible states.) The neutrosophic core (mean) field is the midpoint

$$u_{max}(x,t) = \frac{1}{2}(u_{min}(x,t) + u_{max}(x,t)) \quad (5)$$

and we define two diagnostic functionals:

the absolute width (deterministic spread)

$$W(x,t) = u_{max}(x,t) - u_{min}(x,t) \geq 0 \quad (6)$$

DOI: https://doi.org/10.54216/IJNS.270127

the relative indeterminacy index

$$I(x,t) = \frac{u_{max}(x,t) - u_{min}(x,t)}{|u_{max}(x,t)| + \varepsilon}, \varepsilon > 0\ (small) \qquad (7)$$

Here W quantifies the guaranteed envelope size at each (x,t), while I contextualizes this spread relative to the local core magnitude. The small & prevents division by zero and reflects the practical reality that reliability is inherently poor where the signal is near zero.

Objective 1 (Forward neutrosophic propagation). For prescribed u_0, g_L, g_R, q and intervals (3), compute $\{u_{min}, u_{max}, u_{mean}, W, I\}$ over $(x,t) \in [0,1] \times [0,T]$, and summarize them via:

- spatio-temporal heatmaps of u_{mean} and I.
- "band" profiles $[u_{min}, u_{max}]$ at selected times/locations,
- global and temporal summaries such as percentiles of $I(\cdot,t)$,

$$p_\kappa(t) = inf\{y: mcas\{x \in [0,1]: I(x,t) \le y\} \ge \kappa\} \qquad (8)$$

- coverage curves that quantify the fraction of the space-time domain enjoying a reliability threshold

$$\Phi(\tau) = \frac{1}{|\Omega|}\#\{(x,t) \in [0,1] \times [0,T]: I(x,t) \le \tau\}, |\Omega| = 1 \cdot T \qquad (9)$$

Objective 2 (Sensitivity under indeterminacy). Characterize the sensitivity of salient outputs to (α, S) within (3). For a diagnostic point $x^* \subset (0,1)$ and the final time T, define the response surface

$$R(\alpha,S) = u(x^*,T;\alpha,S), (\alpha,S) \subset [\alpha_{min}, \alpha_{max}] \times [S_{min}, S_{max}] \qquad (10)$$

and visualize/quantify how R varies across the neutrosophic rectangle. This clarifies which parameter is more influential for the observable of interest and where the model is robust vs. fragile.

Objective 3 (Measurement-level reporting). Often decisions depend on sensor readings rather than full fields. Let M be a linear observation operator mapping fields to measurements (e.g., point probes, spatial averages, or time-window integrals):

$$y(\alpha,S) = M[u(\cdot,\cdot;\alpha,S)] \qquad (11)$$

We seek neutrosophic envelopes and reliability indices in the observation space:

$$y_{min} = inf_{(\alpha,S)\in(3)} y(\alpha,S), y_{max} = sup_{(\alpha,S)\in(3)} y(\alpha,S), y_{maxa} = \frac{1}{2}(y_{min} + y_{max}) \qquad (12)$$

$$I_y = \frac{y_{max}(12)^{y_{min}}}{|y_{mean}| + \varepsilon} \qquad (13)$$

These quantities directly inform decisions such as thermal safety margins, actuation thresholds, or calibration priorities.

Assumptions and admissibility. We assume $u_0 \in C^2([0,1]), g_L, g_R \in C^1([0,T])$, and $q \in C([0,1] \times [0,T])$. For each fixed (α,S) the Dirichlet problem (1)-(2) is well-posed with a unique classical solution. The neutrosophic sets (3) are compact and reflect all credible values from prior knowledge, tests, or specifications. When $q \ge 0$ and g_L, g_R are comparable across runs, order preservation of the parabolic operator supports the use of (4) as bona-fide envelopes; for sign-changing q we interpret u_{min}, u_{max} as conservative bounds over the admissible rectangle.

DOI: https://doi.org/10.54216/IJNS.270127

Desired properties of the solution mapping. The reporting quartet (u_{mean}, W, I, Φ) should (i) be interpretable (central tendency + bound + reliability), (ii) be stable under small perturbations of (3) and data, and (iii) localize indeterminacy-i.e., highlight when/where uncertainty genuinely matters (large I) versus where it is negligible (small W and I).

Deliverables. The problem requires producing: (a) the fields (5)-(7) over space-time, (b) summaries (8)-(9), (c) sensitivity portraits (10), and (d) measurement-space envelopes (12)-(13), all computed with respect to the neutrosophic parameter sets (3). This constitutes a complete, decision-oriented characterization of indeterminacy in the heat equation without resorting to unverifiable probabilistic assumptions.

3. Data and Methodology

A. Data

The experiment uses a unit-length one-dimensional bar over a half-unit time interval. Thermal diffusivity and source amplitude are uncertain within the ranges 0.008–0.012 and 0.90–1.10, respectively, to be representative of bounded uncertainty. The initial temperature is a Gaussian warm patch centered at x = 0.20. Heating is provided by a traveling, exponentially decaying Gaussian source whose center oscillates over the domain, generating a traveling thermal blob. Dirichlet boundary conditions are applied to both ends to impose small oscillatory temperatures in order to make the problem nontrivial but controlled. A uniform spatial grid (121 points) and an explicit FTCS time integrator are used with a stability-safe time step chosen against the upper bound of diffusivity. The analysis monitors lower and upper envelopes, their midpoint (core) field, an absolute spread, and a relative indeterminacy index from two extreme runs.

B. Governing relations under neutrosophic inputs

Temperature $u(x,t)$ evolves on $x \in [0,L], t \in [0,T]$ according to the linear parabolic model with a prescribed source $q(x,t)$. Thermal diffusivity α and source amplitude S are treated as indeterminate within admissible intervals $[\underline{\alpha}, \alpha^{-}]$. $[\underline{S}, S^{-}]$. For any (α, S) in those intervals, the strong form is

$$\frac{\partial u}{\partial t}(x,t) = \alpha \frac{\partial^2 u}{\partial x^2}(x,t) + Sq(x,t), (x,t) \in (0,L) \times (0,T] \qquad (14)$$

Initial and boundary data are

$$u(x,0) = u_0(x), Bu(0,t) = g_L(t), Bu(L,t) = g_R(t) \qquad (15)$$

where B may encode Dirichlet, Neumann, or Robin conditions.

C. Space-time discretization

A uniform grid $x_i = i\Delta x$ for $i = 0, \ldots, N_x - 1. \Delta x = L/(N_x - 1)$, and $t_n = n\Delta t, n = 0, \ldots, N_t$. with $N_t \Delta t = T$ is employed. Let $u_i^n \approx u(x_i, t_n)$.

Three consistent schemes are admissible; formulas below enable exact reproduction.

2. Forward-Time Centered-Space (FTCS)

$$u_i^{n+1} = u_i^n + r(u_{i+1}^n - 2u_i^n + u_{i-1}^n) + \Delta t Sq(x_i, t_n), r := \alpha \frac{\Delta t}{\Delta x^2} \qquad (16)$$

Dirichlet data:

$$u_0^{n+1} = g_L(t_{n+1}), u_{N_z-1}^{n+1} = g_R(t_{n+1}) \qquad (17)$$

Stability requires

DOI: https://doi.org/10.54216/IJNS.270127

$$r \le \frac{1}{2} \Leftrightarrow \Delta t \le \frac{\Delta x^2}{2\alpha} \tag{18}$$

To remain stable for all $\alpha \in [\underline{\alpha}, \alpha^-]$, the step is chosen as

$$\Delta t = \theta \frac{\Delta x^2}{2\alpha^-}, 0 < \theta < 1 \tag{19}$$

4. Backward Euler (implicit)

$$u_i^{n+1} - r(u_{i+1}^{n+1} - 2u_i^{n+1} + u_{i-1}^{n+1}) = u_i^n + \Delta t S q(x_i, t_n) \tag{20}$$

with a tridiagonal system per step; unconditionally stable.

5. Crank-Nicolson (CN)

$$u_i^{n+1} - \frac{r}{2}(u_{i+1}^{n+1} - 2u_i^{n+1} + u_{i-1}^{n+1}) = u_i^n + \frac{r}{2}(u_{i+1}^n - 2u_i^n + u_{i-1}^n) + \Delta t S q\left(x_i, t_{n+\frac{1}{2}}\right) \tag{21}$$

Remark (variable coefficients). If $\alpha = \alpha(u)$, substitute $r_i^n := \alpha(u_i^n)\Delta t/\Delta x^2$ into (15) or the half-index form into (19). Robin boundaries $\kappa u + \partial_x u = h$ at $x = 0$ are handled via a ghost point $u^n{}_1 = u_1^n 2\Delta x(\kappa u_0^n - h_L^n)$ (analogously at $x = L$), preserving second-order spatial accuracy.

C. Envelope construction and core/width/indeterminacy

Let $u^n(\alpha, S) \subset R^{N_x}$ be the grid solution after n steps for a specific (α, S). Two extreme runs are performed:

$$u_{min}^n := u^n(\underline{\alpha}, \underline{S}), u_{max}^n := u^n(\alpha^-, S^-) \tag{22}$$

From these, the core, absolute width, and relative indeterminacy index are computed nodewise:

$$u_{mean}^n := \frac{1}{2}(u_{min}^n + u_{max}^n) \tag{23}$$

$$W^n := u_{max}^n - u_{min}^n \ (W^n \ge 0) \tag{24}$$

$$I^n := \frac{W^n}{|u_{mean}^n| + \varepsilon}, \varepsilon > 0 \ (regularizer) \tag{25}$$

Order preservation. For FTCS with (16), the one-step map is a convex combination plus a nonnegative source:

$$u_i^{n+1} = (1 - 2r)u_i^n + ru_{i-1}^n + ru_{i+1}^n + \Delta t S q_i^n \tag{26}$$

Hence $u^n \le v^n \Rightarrow u^{n+1} \le v^{n+1}$. With $S \ge 0$ and $q \ge 0$, increasing α or S does not decrease any component, and the nodewise inequality

$$u_{min}^n \le u_{max}^n \ \forall n \tag{27}$$

follows by induction. Backward Euler and CN share this property under standard M-matrix conditions.

D. Decision-oriented diagnostics

1. Section bands

At a fixed time, level t_n, the spatial band is

DOI: https://doi.org/10.54216/IJNS.270127

$$x_i \mapsto \left[u^n_{min,i}, u^n_{max,i}\right], i = 0, \dots, N_x - 1 \qquad (28)$$

At a sensor location $x = x^*$ (index i^*), the temporal band is $t_n{}' > \left[u^n_{min,i^*}, u^n_{max,i^*}\right]$.

2. Spatial percentiles of the relative indeterminacy

For $\kappa \in (0,1)$, define the κ-quantile of $I(\cdot, t_n)$ over the grid:

$$p_n(t_n) := inf\left\{y : \frac{1}{N_x}\#\{i : I^n_i \le y\} \ge \kappa\right\} \qquad (29)$$

Trajectories $p_{0.50}(t), p_{0.90}(t), p_{0.99}(t)$ summarize median and tail behavior.

3. Coverage of acceptable regions

For a threshold $\tau > 0$, the coverage over space-time is

$$\Phi(\tau) := \frac{1}{N_x(N_t+1)} \sum_{n=0}^{N_t} \sum_{i=0}^{N_x-1} 1\{I^n_i \le \tau\} \qquad (30)$$

This scalar in [0,1] measures the fraction of grid points operating within a desired relative-uncertainty level.

4. Response surfaces and local sensitivities

For a distinguished probe x^* (index i^*) at terminal time T, define

$$R(\alpha, S) := u^{N_t}_i(\alpha, S) \qquad (31)$$

Sampling R on a coarse tensor grid over $[\underline{\alpha}, \alpha^-] \times [\underline{S}, S^-]$ gives a surface that visualizes parameter influence. Around mid-interval parameters (α_m, S_m), central differences provide time-resolved local sensitivities:

$$\frac{\partial u^n_i}{\partial \alpha}|_{(\alpha_m, S_m)} \qquad (32)$$

$$\approx \frac{u^n_i(\alpha_m + h_\alpha, S_m) - u^n_i(\alpha_m - h_\alpha, S_m)}{2h_\alpha} \quad \frac{\partial u^n_i}{\partial S}|_{(\alpha_m, S_m)}$$

$$\approx \frac{u^n_i(\alpha_m, S_m + h_S) - u^n_i(\alpha_m, S_m - h_S)}{2h_S} \qquad (33)$$

E. Multiple uncertain inputs and dependency control

If additional parameters are indeterminate (e.g., thermal contact resistance R_c, boundary heat-flux amplitude H), naive interval arithmetic can over-inflate bounds. Two practical strategies are recommended:

Corner sweep: solve at all vertices of the parameter hyper-rectangle $\Theta = \prod_{k=1}^{P} \left[\underline{\theta_k}, \theta^-{}_k\right]$ and take pointwise min/max :

$$u_{min}(x_i, t_n) = \min_{\theta \in \theta_{commax}} u(x_i, t_n; \theta) \qquad (34)$$

$$u_{max}(x_i, t_n) = \max_{\theta \subset \theta_{commax}} u(x_i, t_n; \theta) \qquad (35)$$

Affine surrogate (first-order): for small intervals, linearize around θ_m and bound the linear form:

$$u(x_i, t_n; \theta) \approx u(x_i, t_n; \theta_m) + \sum_{k=1}^{P} \frac{\partial u}{\partial \theta_k}(x_i, t_n; \theta_m)\left(\theta_k - \theta_{k,m}\right) \qquad (36)$$

DOI: https://doi.org/10.54216/IJNS.270127

Upper/lower bounds follow by assigning each $(\theta_k - \theta_{k,m})$ to its interval endpoint with the sign of the sensitivity.

F. Error, stability, and verification

For sufficiently smooth solutions, global errors obey classical orders:

$$\text{FTCS:} \|u(\cdot, t_n) - u^n\|_\infty \leq C(T)(\Delta t + \Delta x^2) \quad (37)$$

$$CN: \|u(\cdot, t_n) - u^n\|_\infty \leq C(T)(\Delta t^2 + \Delta x^2) \quad (38)$$

Because u_{mean} and W are linear combinations/differences of two solutions, the same orders transfer to those quantities. The relative index I is stable away from $u_{mean} = 0$; the regularizer ε , prevents blowup and should be tied to sensor resolution.

6. Result

Set up the 1-D heat model with given IC/BC, moving source $q(x, t)$, and neutrosophic intervals for α and S. Solve the PDE twice at the interval corners $(\underline{\alpha}, \underline{S})$ and (α^-, S^-) to obtain u_{min} and u_{max} on a stable FTCS grid.

Post-process to compute $u_{mean} = \frac{1}{2}(u_{min} + u_{max})$, spread $W = u_{max} - u_{min}$, and R|I $= W/(|u_{mean}| + \varepsilon)$, then plot sections, percentiles, coverage, and response surfaces.

Figure 1 presents (a) Mean Temperature$u_{mean}(x, t)$: Shows the core (midpoint) solution of the neutrosophic heat equation over $x \in [0,1], t \in [0,0.5]$. The warm ridge near $x \approx 0.2$ at early times comes from the moving, decaying Gaussian source; color fades as diffusion and source decay reduce amplitude. Light boundary bands reflect the small oscillatory Dirichlet conditions. (b) Width $W(x, t) = u_{max} - u_{min}$: Quantifies absolute uncertainty due to $\alpha \in [0.008,0.012]$ and $S \in [0.90,1.10]$. Width is small over most of the domain, peaking in a diagonal stripe that tracks the source's path and near boundaries when forcing aligns with steep gradients. Notably, largest W does not coincide with the largest mean temperature everywhere, highlighting that uncertainty localizes around fronts and interaction regions rather than global peaks.

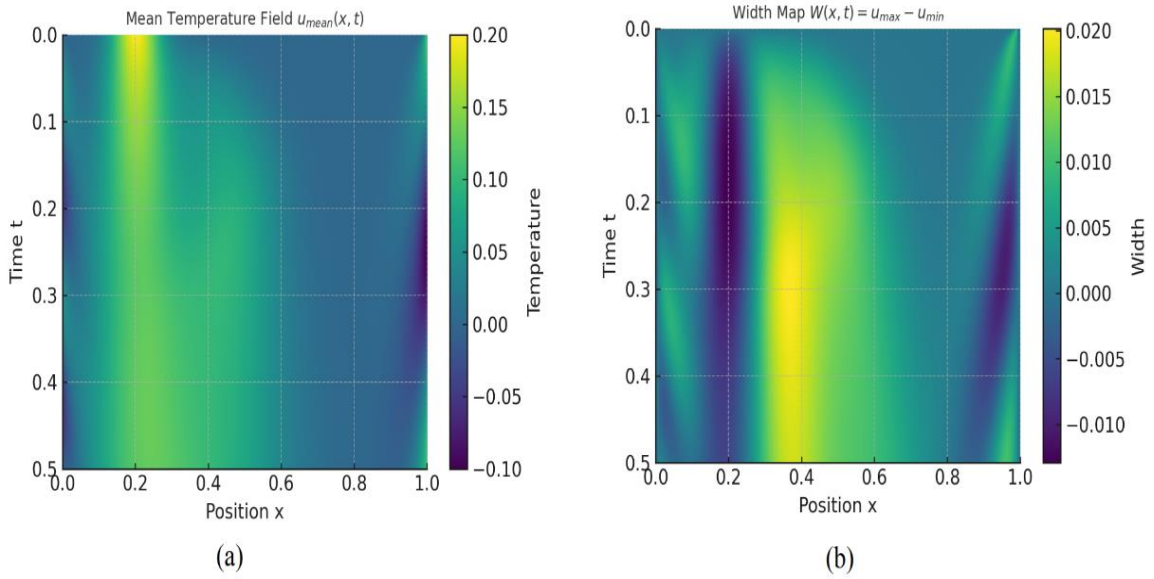

Figure 1. Mean Field and Uncertainty Width (space-time maps).

DOI: https://doi.org/10.54216/IJNS.270127

Figures 2 presents (a): Response surface $u(0.5, T)$ vs. (α, S): Shows the terminal temperature at the mid-point $x = 0.5$ as diffusivity α and source amplitude S vary over their admissible ranges. The surface rises monotonically with S, indicating stronger sensitivity to source strength. Dependence on α is mild and slightly non-monotonic due to the balance between faster diffusion (which flattens peaks) and quicker transport toward the probe over the finite horizon.

(b) Lower envelope $u_{min}(x, t)$: Displays the space-time temperature obtained at the most conservative corner (α_{min}, S_{min}). The moving warm region is present but weaker and more diffuse than in the mean field, as expected with the smallest source and slowest diffusion. This panel provides a guaranteed lower bound on temperature everywhere for the specified parameter intervals.

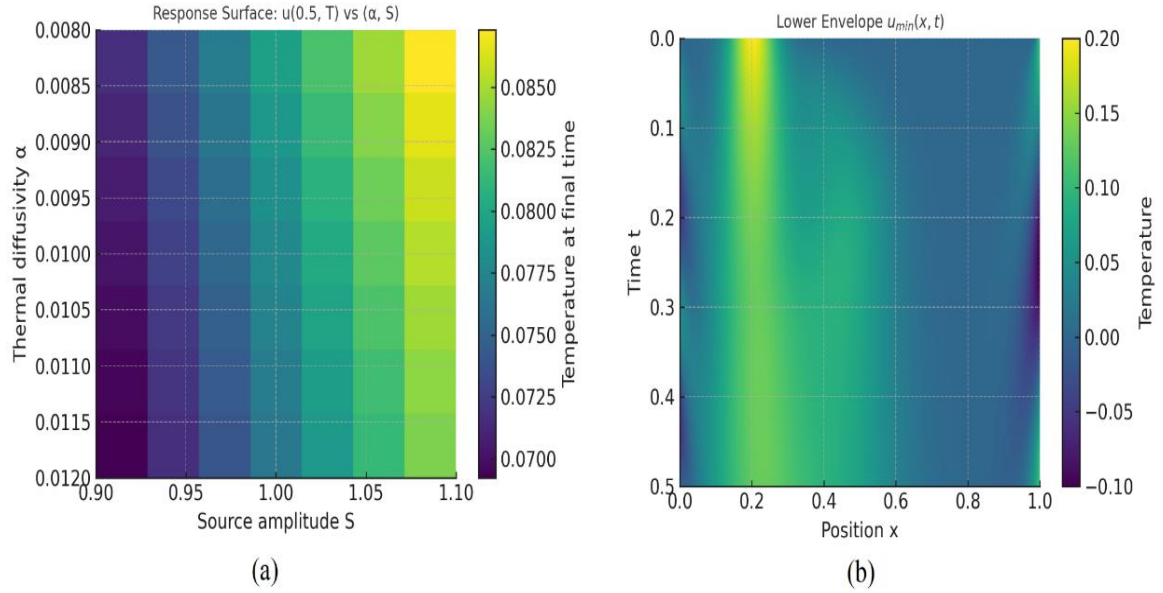

Figure 2. Parameter Response and Lower Envelope.

Figure 3 shows multi-panel figure summarizes the behavior of the neutrosophic envelopes along sample space time slices. The mid-time spatial profile at $t = 0.25$ has a smooth mean temperature and a narrow uncertainty band that widens near the moving-source center and tightens toward the boundaries. The left-boundary time series conveys an oscillatory signal driven by the Dirichlet forcing; the band is narrow except in the neighborhood of zero-crossings. At the domain center x=0.5, the mean temperature rises during the passage of the heat pulse and then remains flat, with merely a narrow band during the brief passage time. Space-averaged temperature versus time rises rapidly, then slowly, indicating global measures to be unresponsive to parameter ranges. The time-averaged spatial profile peaks where the source takes longest to reside, while the final-time profile contains a broad bump with slightly broader bands near the interior front. The bottom panel provides $t^*(x)$, the moment of peak relative indeterminacy at every point; crisp peaks correspond to advancing and receding fronts of the thermal pulse and to boundary-caused sign reversals, showing where reliability is most vulnerable along the road.

DOI: https://doi.org/10.54216/IJNS.270127

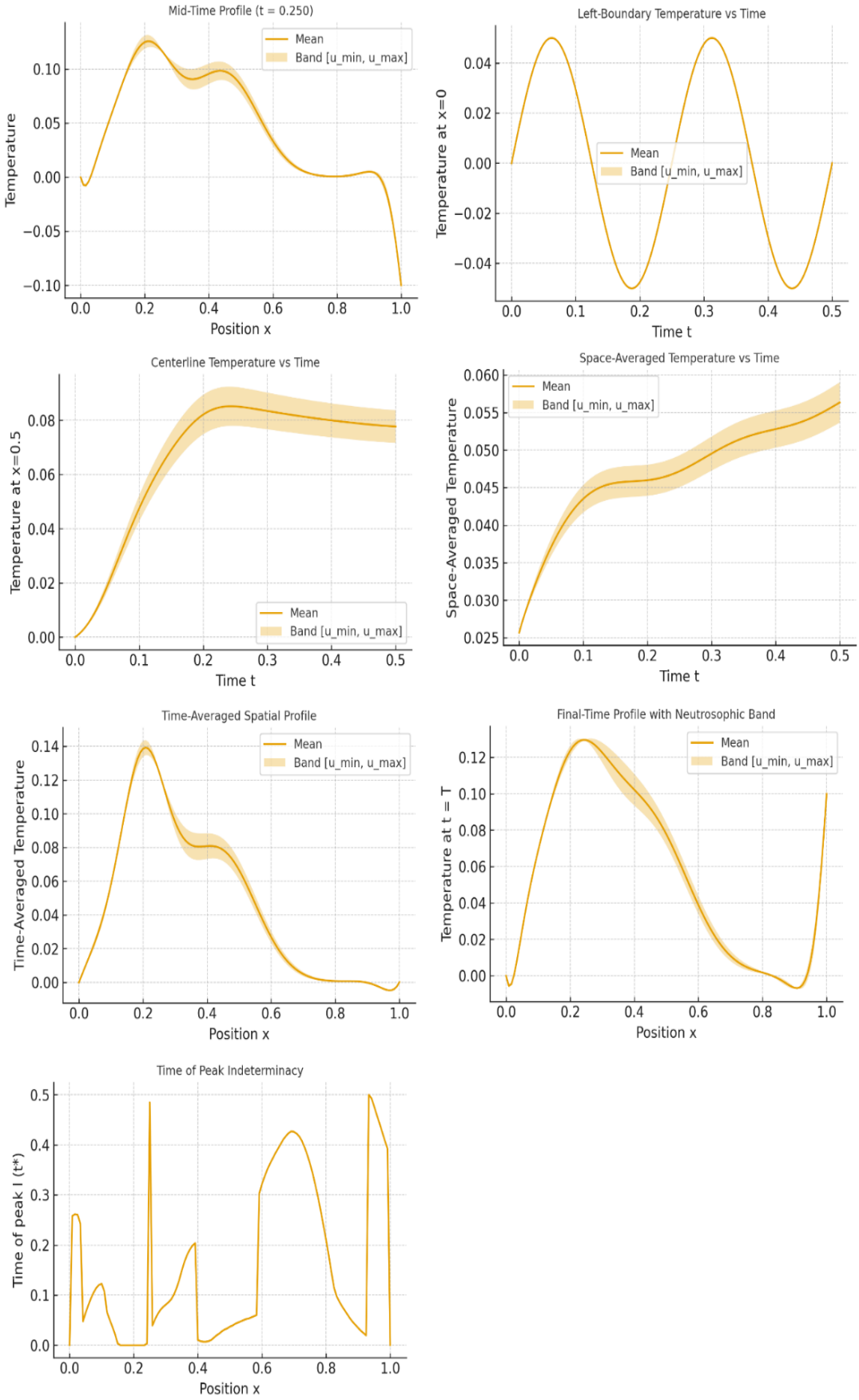

Figure 3. Section Bands, Aggregates, and Peak-Indeterminacy Timing.

DOI: https://doi.org/10.54216/IJNS.270127

Tracks the absolute envelope width $W = u_{max} - u_{min}$ over time using the median, 90th, and 99th percentiles across space. All curves rise as the heat pulse traverses the rod and parameter effects accumulate, with the tail (99th) peaking around $t \approx 0.30$ and then gently declining as diffusion and source decay reduce contrasts. The median remains an order of magnitude smaller, confirming that most locations experience tight envelopes.

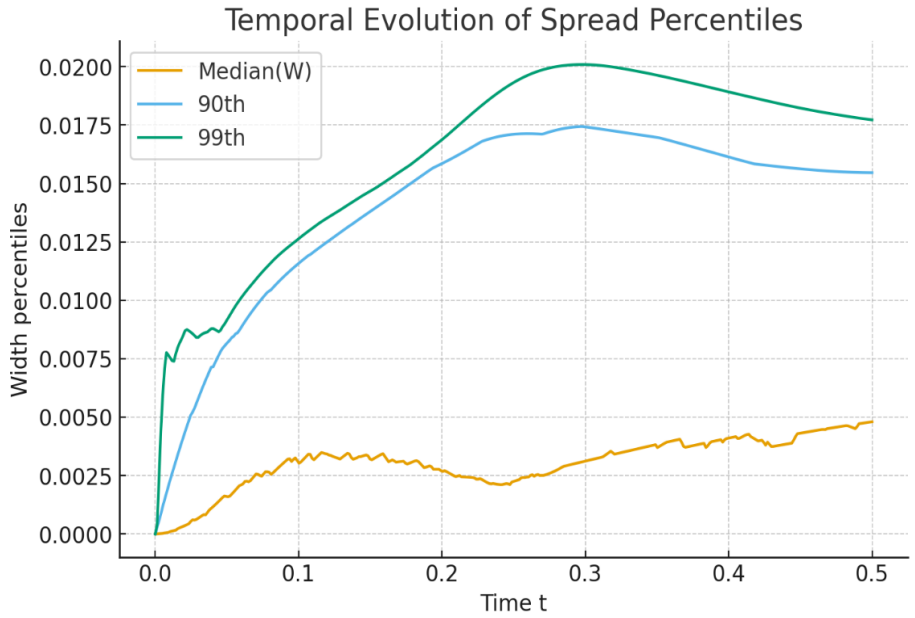

Figure 4. Temporal Evolution of Spread Percentiles.

Figure 5 Shows how the magnitude of the core field evolves. The upper percentiles gradually decrease early (source decay and diffusion) and then flatten, whereas the median increases as the hotspot reaches more of the domain before leveling off. Together with Fig. 4, these trends explain why relative uncertainty spikes only when $|u_{mean}|$ becomes small.

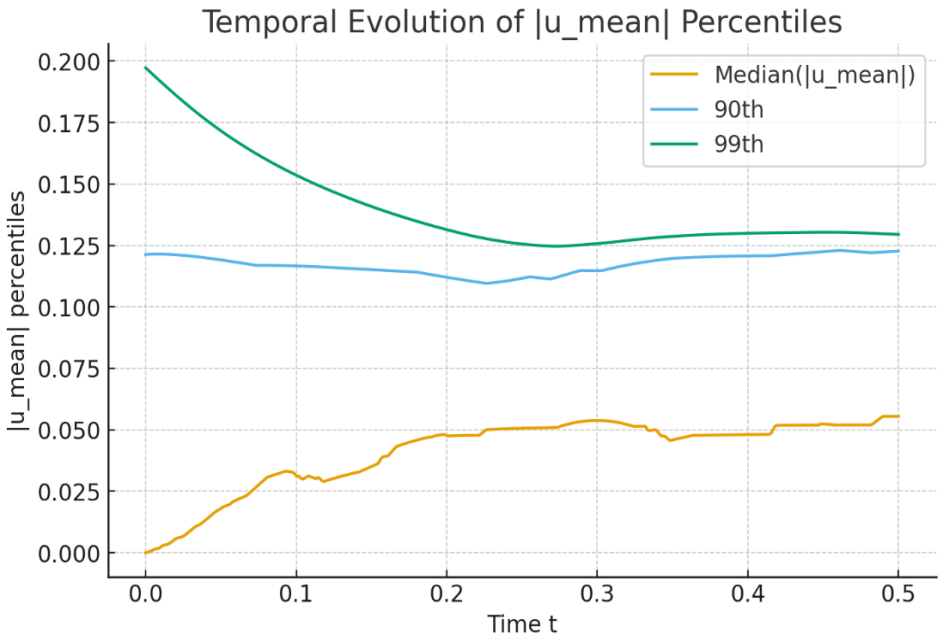

Figure 5. Temporal Evolution of $|u_{mean}|$ Percentiles.

DOI: https://doi.org/10.54216/IJNS.270127

Presents percentiles of the relative indeterminacy index $RII = W/(|u_{mean}| + \varepsilon)$. The median stays low and stable, indicating broad reliability; the 90th percentile hovers below one. The 99th percentile exhibits sharp, short-lived spikes near zero-crossings of the core field, highlighting rare but pronounced local reliability losses.

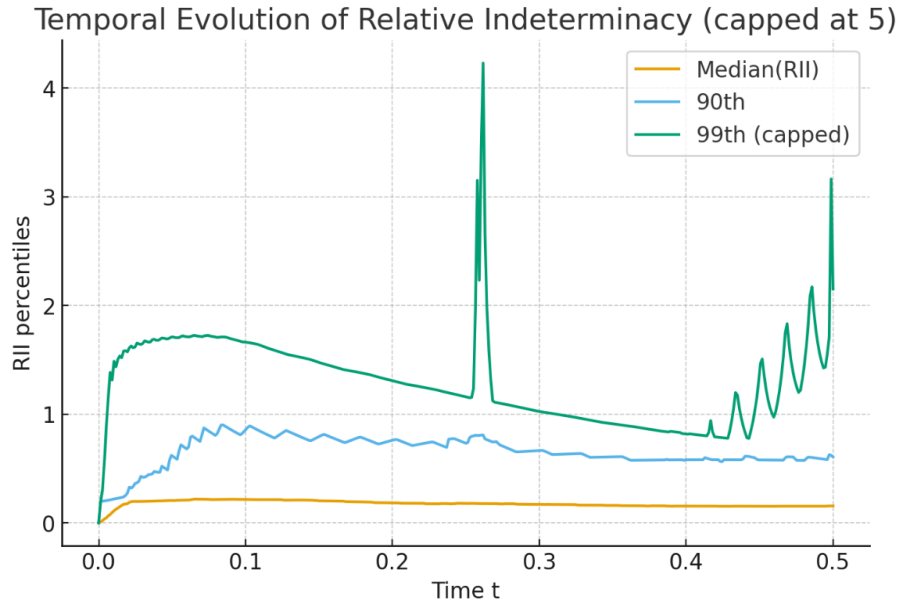

Figure 6. Temporal Evolution of Relative Indeterminacy (capped at 5).

Compares final-time temperature $u(x, T)$ for five α values. Larger diffusivity slightly lowers the peak and spreads heat, producing smoother profiles with minor phase changes; differences are modest relative to those driven by S. The overall shape-peak near $x \approx 0.25$ and small boundary features-remains consistent.

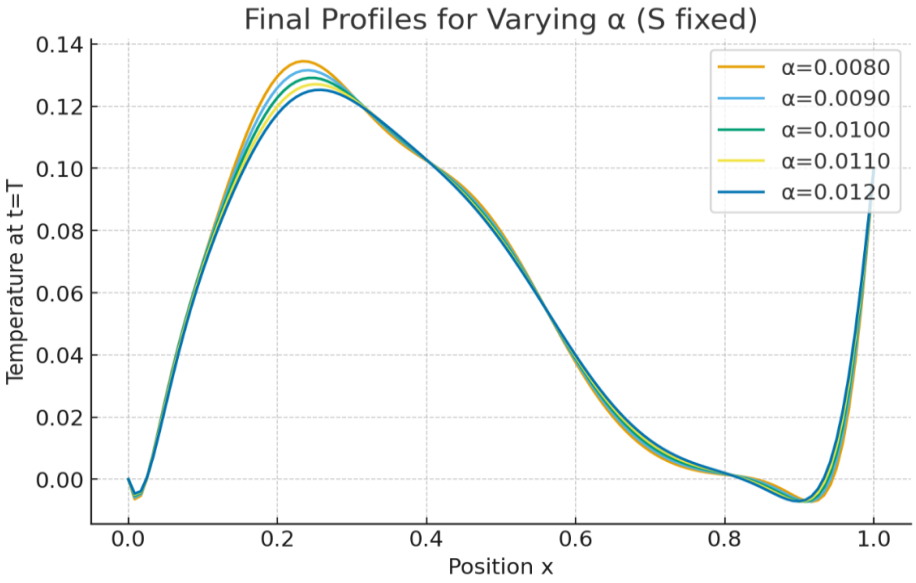

Figure 7. Final Profiles for Varying Diffusivity α (Source S fixed).

Displays $u(0.5, t)$ as S varies. Curves scale primarily with S : higher source amplitude raises the peak and the late-time plateau with little change in timing, confirming that amplitude governs magnitude while geometry and boundary forcing set the trajectory shape. This complements Fig. 7 by showing stronger sensitivity to S than to α for the chosen horizon.

DOI: https://doi.org/10.54216/IJNS.270127

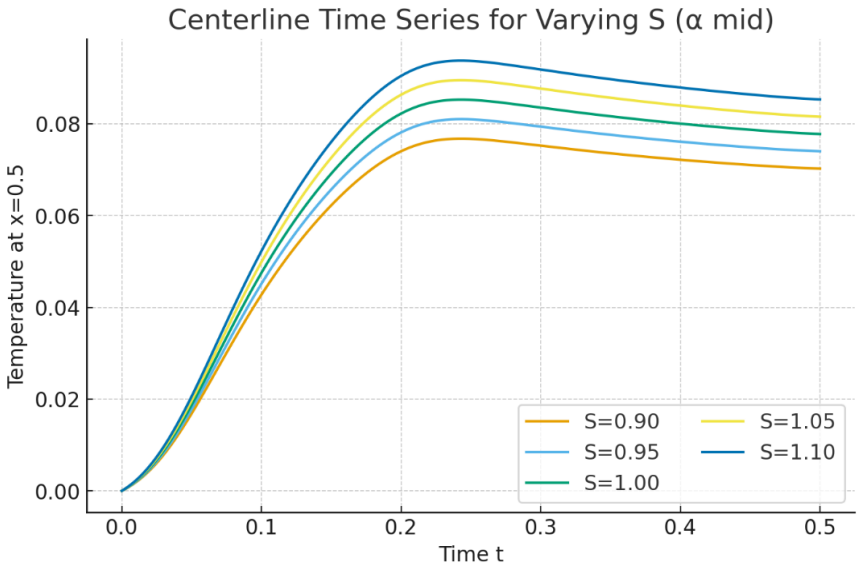

Figure 8. Centerline Time Series for Varying Source Amplitude S (α at mid-interval).

6. Conclusion

A neutrosophic transient heat equation model was built where thermal diffusivity and source amplitude are defined as admissible intervals. Optimization of the model at parameter extremes results in guaranteed temperature envelopes $[u_{min}, u_{max}]$, A mean field u_{mean} and an absolute spread W, along with a relative indeterminacy index (RII) provide an interpretable overview of state and reliability. Absolute spreads are small across the enormous majority of the space time domain during the course of the experiments, but large RII appears only in thin, transient areas essentially at near-zero-crossings of the core field and along the moving and returning fronts of the traveling source. Percentile traces and coverage plots demonstrate that the majority of the domain is operating inside moderate uncertainty boundaries, with sporadic, transient invasions captured by the 99th-percentile spikes.

Sensitivity analyses indicate higher sensitivity of end and centreline temperatures to source amplitude than to diffusivity across the chosen horizon; diffusivity in effect reverses smoothing and phase, whereas the source determines amplitude. This precedence guides calibration and sensing priorities when resources are limited in the direction of source characterization. Response surfaces, section bands, and exceedance maps transform interval inputs into actionable reliability margins, specifying where and when operating tolerances may be relaxed or additional data need to be obtained.

It is solver-independent, convergent, and stable, with the additional cost of two deterministic solves and minimal post-processing. Current scope is linear source-one-dimensional with natural extensions to temperature-dependent coefficients, higher dimensions in geometry, additional uncertain parameters (e.g., contact resistance), and coupling to thermo-mechanical risk metrics such as thermal shock. Overall, neutrosophic propagation offers a conservative and transparent basis for heat-transfer prediction with limited information so transparent, defendable decisions can be made in analysis, design, and control.

Funding: "This research received no external funding"

Conflicts of Interest: "The authors declare no conflict of interest."

References

[1] L. E. Frenzel, *Crash Course in Electronics Technology*, 2nd ed. Oxford, U.K.: Newnes, 1997.

[2] J.-C. Han and B.-L. Wang, "Thermal shock resistance of ceramics with temperature-dependent material properties at elevated temperature," *Acta Materialia*, vol. 59, pp. 1373–1382, 2011.

[3] C. Luo, T. Jiao, J. Gu, Y. Tang, and J. Kong, "Graphene shield by SiBCN ceramic: A promising high-temperature electromagnetic wave-absorbing material with oxidation resistance," *ACS Applied Materials & Interfaces*, vol. 10, pp. 39307–39318, 2018.

DOI: https://doi.org/10.54216/IJNS.270127

[4] N. Van Garderen, F. J. Clemens, M. Mezzomo, C. P. Bergmann, and T. Graule, "Investigation of clay content and sintering temperature on attrition resistance of highly porous diatomite-based material," *Applied Clay Science*, vol. 52, pp. 115–121, 2011.

[5] A. M. Khounsary, D. Chojnowski, L. Assoufid, and W. M. Worek, *High Heat Flux and Synchrotron Radiation Beamlines*, pp. 45–51. Bellingham, WA, USA: International Society for Optics and Photonics (SPIE), 1997.

[6] D. Liu, Y. Luo, and X. Shang, "Experimental investigation of high temperature thermal contact resistance between high thermal conductivity C/C material and Inconel 600," *International Journal of Heat and Mass Transfer*, vol. 80, pp. 407–410, 2015.

[7] F. Shahzad, A. Iqbal, H. Kim, and C. M. Koo, "2D transition metal carbides (MXenes): Applications as an electrically conducting material," *Advanced Materials*, vol. 32, 2002159, 2020.

[8] R.-B. Hong, J.-R. Wu, and H.-B. Cai, "Low-temperature crack resistance of coal gangue powder and polyester fibre asphalt mixture," *Construction and Building Materials*, vol. 238, 117678, 2020.

[9] M. Aslam, "A study on skewness and kurtosis estimators of wind speed distribution under indeterminacy," *Theoretical and Applied Climatology*, vol. 143, pp. 1227–1234, 2021.

[10] P. Grzegorzewski, "Testing statistical hypotheses with vague data," *Fuzzy Sets and Systems*, vol. 112, pp. 501–510, 2000.

[11] R. A. K. Sherwani, H. Shakeel, W. B. Awan, M. Faheem, and M. Aslam, "Analysis of COVID-19 data using neutrosophic Kruskal–Wallis H test," *BMC Medical Research Methodology*, vol. 21, pp. 1–7, 2021.

[12] J. Chen, J. Ye, and S. Du, "Scale effect and anisotropy analyzed for neutrosophic numbers of rock joint roughness coefficient based on neutrosophic statistics," *Symmetry*, vol. 9, p. 208, 2017.

[13] J. Ye, "Improved cosine similarity measures of simplified neutrosophic sets for medical diagnoses," *Artificial Intelligence in Medicine*, vol. 63, pp. 171–179, 2015.

[14] M. Aslam, "Enhanced statistical tests under indeterminacy with application to earth speed data," *Earth Science Informatics*, vol. 14, pp. 1261–1267, 2021.

[15] F. Smarandache, *The Neutrosophic Research Method in Scientific and Humanistic Fields*. Albuquerque, NM, USA: The College of Information Sciences and Technology, 2010.

[16] A. M. Alzahrani, M. K. A. Khan, and F. Smarandache, "Neutrosophic set theory and its applications in decision-making processes," *Mathematics*, vol. 9, no. 10, p. 1128, 2021.

[17] M. G. G. Chico, N. H. Bandera, S. H. Lazo, and N. L. Sailema, "Assessment of the relevance of intercultural medical care. Neutrosophic sampling," *Neutrosophic Sets and Systems*, vol. 44, pp. 420–426, 2021.

[18] R. A. K. Sherwani, H. Shakeel, W. B. Awan, M. Faheem, and M. Aslam, "Analysis of COVID-19 data using neutrosophic Kruskal–Wallis H test," *BMC Medical Research Methodology*, vol. 21, pp. 1–7, 2021.

[19] O. G. El Barbary and R. Abu Gdairi, "Neutrosophic logic-based document summarization," *Journal of Mathematics*, 2021, pp. 1–7.

[20] W.-Q. Duan, Z. Khan, M. Gulistan, and A. Khurshid, "Neutrosophic exponential distribution: Modeling and applications for complex data analysis," *Complexity*, 2021, pp. 1–8.

[21] M. Gulistan, A. Elmoasry, and N. Yaqoob, "N-version of the neutrosophic cubic set: Application in the negative influences of Internet," *The Journal of Supercomputing*, vol. 77, p. 11410, 2021.

[22] M. Aslam, "A new attribute sampling plan using neutrosophic statistical interval method," *Complex & Intelligent Systems*, vol. 5, pp. 365–370, 2019.

[23] F. Smarandache, *Introduction to Neutrosophic Statistics*. Craiova, Romania: Infinite Study (Romania-Educational Publisher), 2014.

[24] J. Chen, J. Ye, and S. Du, "Scale effect and anisotropy analyzed for neutrosophic numbers of rock joint roughness coefficient based on neutrosophic statistics," *Symmetry*, vol. 9, p. 208, 2017.

DOI: https://doi.org/10.54216/IJNS.270127

[25] J. Chen, J. Ye, S. Du, and R. Yong, "Expressions of rock joint roughness coefficient using neutrosophic interval statistical numbers," *Symmetry*, vol. 9, p. 123, 2017.

[26] M. Aslam, "Design of the Bartlett and Hartley tests for homogeneity of variances under indeterminacy environment," *Journal of Taibah University for Science*, vol. 14, pp. 6–10, 2020.

[27] M. Aslam, "On detecting outliers in complex data using Dixon's test under neutrosophic statistics," *Journal of King Saud University – Science*, vol. 32, pp. 2005–2008, 2020.

[28] A. Bid, A. Bora, and A. Raychaudhuri, "Temperature dependence of the resistance of metallic nanowires of diameter ≥ 15 nm: Applicability of Bloch–Grüneisen theorem," *Physical Review B*, vol. 74, 035426, 2006.

[29] J. Elguindi, J. Wagner, and C. Rensing, "Genes involved in copper resistance influence survival of *Pseudomonas aeruginosa* on copper surfaces," *Journal of Applied Microbiology*, vol. 106, pp. 1448–1455, 2009.

[30] N. Almusallam, B. T. AlNuaimi, H. Alkattan, M. Abotaleb, and K. Dhoska, "Physics-informed neural networks for solving the heat equation in thermal engineering," *International Journal of Technical and Physical Problems of Engineering*, vol. 17, no. 1, pp. 375–382, 2025.

DOI: https://doi.org/10.54216/IJNS.270127